

Measurement of inclusive electrons from open heavy-flavor hadron decays in $p+p$ collisions at $\sqrt{s} = 200$ GeV with the STAR detector

M. S. Abdallah,⁵ B. E. Aboona,⁵⁵ J. Adam,⁶ L. Adamczyk,² J. R. Adams,³⁹ J. K. Adkins,³⁰ G. Agakishiev,²⁸ I. Aggarwal,⁴¹ M. M. Aggarwal,⁴¹ Z. Ahammed,⁶⁰ I. Alekseev,^{3,35} D. M. Anderson,⁵⁵ A. Aparin,²⁸ E. C. Aschenauer,⁶ M. U. Ashraf,¹¹ F. G. Atetalla,²⁹ A. Attri,⁴¹ G. S. Averichev,²⁸ V. Bairathi,⁵³ W. Baker,¹⁰ J. G. Ball Cap,²⁰ K. Barish,¹⁰ A. Behera,⁵² R. Bellwied,²⁰ P. Bhagat,²⁷ A. Bhasin,²⁷ J. Bielcik,¹⁴ J. Bielcikova,³⁸ I. G. Bordyuzhin,³ J. D. Brandenburg,⁶ A. V. Brandin,³⁵ I. Bunzarov,²⁸ X. Z. Cai,⁵⁰ H. Caines,⁶³ M. Calderón de la Barca Sánchez,⁸ D. Cebra,⁸ I. Chakaberia,^{31,6} P. Chaloupka,¹⁴ B. K. Chan,⁹ F-H. Chang,³⁷ Z. Chang,⁶ N. Chankova-Bunzarova,²⁸ A. Chatterjee,¹¹ S. Chattopadhyay,⁶⁰ D. Chen,¹⁰ J. Chen,⁴⁹ J. H. Chen,¹⁸ X. Chen,⁴⁸ Z. Chen,⁴⁹ J. Cheng,⁵⁷ M. Chevalier,¹⁰ S. Choudhury,¹⁸ W. Christie,⁶ X. Chu,⁶ H. J. Crawford,⁷ M. Csanád,¹⁶ M. Daugherty,¹ T. G. Dedovich,²⁸ I. M. Deppner,¹⁹ A. A. Derevschikov,⁴³ A. Dhamija,⁴¹ L. Di Carlo,⁶² L. Didenko,⁶ P. Dixit,²² X. Dong,³¹ J. L. Drachenberg,¹ E. Duckworth,²⁹ J. C. Dunlop,⁶ N. Elsey,⁶² J. Engelage,⁷ G. Eppley,⁴⁵ S. Esumi,⁵⁸ O. Evdokimov,¹² A. Ewigleben,³² O. Eyser,⁶ R. Fatemi,³⁰ F. M. Fawzi,⁵ S. Fazio,⁶ P. Federic,³⁸ J. Fedorisin,²⁸ C. J. Feng,³⁷ Y. Feng,⁴⁴ P. Filip,²⁸ E. Finch,⁵¹ Y. Fisyak,⁶ A. Francisco,⁶³ C. Fu,¹¹ L. Fulek,² C. A. Gagliardi,⁵⁵ T. Galatyuk,¹⁵ F. Geurts,⁴⁵ N. Ghimire,⁵⁴ A. Gibson,⁵⁹ K. Gopal,²³ X. Gou,⁴⁹ D. Grosnick,⁵⁹ A. Gupta,²⁷ W. Guryn,⁶ A. I. Hamad,²⁹ A. Hamed,⁵ Y. Han,⁴⁵ S. Harabasz,¹⁵ M. D. Harasty,⁸ J. W. Harris,⁶³ H. Harrison,³⁰ S. He,¹¹ W. He,¹⁸ X. H. He,²⁶ Y. He,⁴⁹ S. Heppelmann,⁸ S. Heppelmann,⁴² N. Herrmann,¹⁹ E. Hoffman,²⁰ L. Holub,¹⁴ Y. Hu,¹⁸ H. Huang,³⁷ H. Z. Huang,⁹ S. L. Huang,⁵² T. Huang,³⁷ X. Huang,⁵⁷ Y. Huang,⁵⁷ T. J. Humanic,³⁹ G. Igo,^{9,*} D. Isenhower,¹ W. W. Jacobs,²⁵ C. Jena,²³ A. Jentsch,⁶ Y. Ji,³¹ J. Jia,^{6,52} K. Jiang,⁴⁸ X. Ju,⁴⁸ E. G. Judd,⁷ S. Kabana,⁵³ M. L. Kabir,¹⁰ S. Kagamaster,³² D. Kalinkin,^{25,6} K. Kang,⁵⁷ D. Kapukchyan,¹⁰ K. Kauder,⁶ H. W. Ke,⁶ D. Keane,²⁹ A. Kechechyan,²⁸ M. Kelsey,⁶² Y. V. Khyzhniak,³⁵ D. P. Kikoła,⁶¹ C. Kim,¹⁰ B. Kimelman,⁸ D. Kincses,¹⁶ I. Kisel,¹⁷ A. Kiselev,⁶ A. G. Knospe,³² H. S. Ko,³¹ L. Kochenda,³⁵ L. K. Kosarzewski,¹⁴ L. Kramarik,¹⁴ P. Kravtsov,³⁵ L. Kumar,⁴¹ S. Kumar,²⁶ R. Kunnawalkam Elayavalli,⁶³ J. H. Kwasizur,²⁵ R. Lacey,⁵² S. Lan,¹¹ J. M. Landgraf,⁶ J. Lauret,⁶ A. Lebedev,⁶ R. Lednicky,^{28,38} J. H. Lee,⁶ Y. H. Leung,³¹ C. Li,⁴⁹ C. Li,⁴⁸ W. Li,⁴⁵ X. Li,⁴⁸ Y. Li,⁵⁷ X. Liang,¹⁰ Y. Liang,²⁹ R. Licenik,³⁸ T. Lin,⁴⁹ Y. Lin,¹¹ M. A. Lisa,³⁹ F. Liu,¹¹ H. Liu,²⁵ H. Liu,¹¹ P. Liu,⁵² T. Liu,⁶³ X. Liu,³⁹ Y. Liu,⁵⁵ Z. Liu,⁴⁸ T. Ljubicic,⁶ W. J. Llope,⁶² R. S. Longacre,⁶ E. Loyd,¹⁰ N. S. Lukow,⁵⁴ X. F. Luo,¹¹ L. Ma,¹⁸ R. Ma,⁶ Y. G. Ma,¹⁸ N. Magdy,¹² D. Mallick,³⁶ S. Margetis,²⁹ C. Markert,⁵⁶ H. S. Matis,³¹ J. A. Mazer,⁴⁶ N. G. Minaev,⁴³ S. Mioduszewski,⁵⁵ B. Mohanty,³⁶ M. M. Mondal,⁵² I. Mooney,⁶² D. A. Morozov,⁴³ A. Mukherjee,¹⁶ M. Nagy,¹⁶ J. D. Nam,⁵⁴ Md. Nasim,²² K. Nayak,¹¹ D. Neff,⁹ J. M. Nelson,⁷ D. B. Nemes,⁶³ M. Nie,⁴⁹ G. Nigmatkulov,³⁵ T. Niida,⁵⁸ R. Nishitani,⁵⁸ L. V. Nogach,⁴³ T. Nonaka,⁵⁸ A. S. Nunes,⁶ G. Odyniec,³¹ A. Ogawa,⁶ S. Oh,³¹ V. A. Okorokov,³⁵ B. S. Page,⁶ R. Pak,⁶ J. Pan,⁵⁵ A. Pandav,³⁶ A. K. Pandey,⁵⁸ Y. Panebratsev,²⁸ P. Parfenov,³⁵ B. Pawlik,⁴⁰ D. Pawlowska,⁶¹ H. Pei,¹¹ C. Perkins,⁷ L. Pinsky,²⁰ R. L. Pintér,¹⁶ J. Pluta,⁶¹ B. R. Pokhrel,⁵⁴ G. Pomatkin,³⁸ J. Porter,³¹ M. Posik,⁵⁴ V. Prozorova,¹⁴ N. K. Pruthi,⁴¹ M. Przybycien,² J. Putschke,⁶² H. Qiu,²⁶ A. Quintero,⁵⁴ C. Racz,¹⁰ S. K. Radhakrishnan,²⁹ N. Raha,⁶² R. L. Ray,⁵⁶ R. Reed,³² H. G. Ritter,³¹ M. Robotkova,³⁸ O. V. Rogachevskiy,²⁸ J. L. Romero,⁸ D. Roy,⁴⁶ L. Ruan,⁶ J. Rusnak,³⁸ N. R. Sahoo,⁴⁹ H. Sako,⁵⁸ S. Salur,⁴⁶ J. Sandweiss,^{63,*} S. Sato,⁵⁸ W. B. Schmidke,⁶ N. Schmitz,³³ B. R. Schweid,⁵² F. Seck,¹⁵ J. Seger,¹³ M. Sergeeva,⁹ R. Seto,¹⁰ P. Seyboth,³³ N. Shah,²⁴ E. Shahaliev,²⁸ P. V. Shanmuganathan,⁶ M. Shao,⁴⁸ T. Shao,¹⁸ A. I. Sheikh,²⁹ D. Shen,⁵⁰ S. S. Shi,¹¹ Y. Shi,⁴⁹ Q. Y. Shou,¹⁸ E. P. Sichtermann,³¹ R. Sikora,² M. Simko,³⁸ J. Singh,⁴¹ S. Singha,²⁶ M. J. Skoby,⁴⁴ N. Smirnov,⁶³ Y. Söhnngen,¹⁹ W. Solyst,²⁵ P. Sorensen,⁶ H. M. Spinka,^{4,*} B. Srivastava,⁴⁴ T. D. S. Stanislaus,⁵⁹ M. Stefaniak,⁶¹ D. J. Stewart,⁶³ M. Strikhanov,³⁵ B. Stringfellow,⁴⁴ A. A. P. Suaide,⁴⁷ M. Sumera,³⁸ B. Summa,⁴² X. M. Sun,¹¹ X. Sun,¹² Y. Sun,⁴⁸ Y. Sun,²¹ B. Surrow,⁵⁴ D. N. Svirida,³ Z. W. Sweger,⁸ P. Szymanski,⁶¹ A. H. Tang,⁶ Z. Tang,⁴⁸ A. Taranenko,³⁵ T. Tarnowsky,³⁴ J. H. Thomas,³¹ A. R. Timmins,²⁰ D. Tlusty,¹³ T. Todoroki,⁵⁸ M. Tokarev,²⁸ C. A. Tomkiel,³² S. Trentalange,⁹ R. E. Tribble,⁵⁵ P. Tribedy,⁶ S. K. Tripathy,¹⁶ T. Truhlar,¹⁴ B. A. Trzeciak,¹⁴ O. D. Tsai,⁹ Z. Tu,⁶ T. Ullrich,⁶ D. G. Underwood,^{4,59} I. Upsal,⁴⁵ G. Van Buren,⁶ J. Vanek,³⁸ A. N. Vasiliev,⁴³ I. Vassiliev,¹⁷ V. Verkest,⁶² F. Videbæk,⁶ S. Vokal,²⁸ S. A. Voloshin,⁶² F. Wang,⁴⁴ G. Wang,⁹ J. S. Wang,²¹ P. Wang,⁴⁸ Y. Wang,¹¹ Y. Wang,⁵⁷ Z. Wang,⁴⁹ J. C. Webb,⁶ P. C. Weidenkaff,¹⁹ L. Wen,⁹ G. D. Westfall,³⁴ H. Wieman,³¹ S. W. Wissink,²⁵ J. Wu,²⁶ Y. Wu,¹⁰ B. Xi,⁵⁰ Z. G. Xiao,⁵⁷ G. Xie,³¹ W. Xie,⁴⁴ H. Xu,²¹ N. Xu,³¹ Q. H. Xu,⁴⁹ Y. Xu,⁴⁹ Z. Xu,⁶ Z. Xu,⁹ C. Yang,⁴⁹ Q. Yang,⁴⁹ S. Yang,⁴⁵ Y. Yang,³⁷ Z. Ye,⁴⁵ Z. Ye,¹² L. Yi,⁴⁹ K. Yip,⁶ Y. Yu,⁴⁹ H. Zbroszczyk,⁶¹ W. Zha,⁴⁸ C. Zhang,⁵² D. Zhang,¹¹ J. Zhang,⁴⁹ S. Zhang,¹² S. Zhang,¹⁸ X. P. Zhang,⁵⁷ Y. Zhang,²⁶ Y. Zhang,⁴⁸ Y. Zhang,¹¹ Z. J. Zhang,³⁷ Z. Zhang,⁶ Z. Zhang,¹² J. Zhao,⁴⁴ C. Zhou,¹⁸ X. Zhu,⁵⁷ M. Zurek,⁴ and M. Zyzak¹⁷

(STAR Collaboration)

- ¹Abilene Christian University, Abilene, Texas 79699
- ²AGH University of Science and Technology, FPACS, Cracow 30-059, Poland
- ³Alikhanov Institute for Theoretical and Experimental Physics NRC "Kurchatov Institute", Moscow 117218, Russia
- ⁴Argonne National Laboratory, Argonne, Illinois 60439
- ⁵American University of Cairo, New Cairo 11835, New Cairo, Egypt
- ⁶Brookhaven National Laboratory, Upton, New York 11973
- ⁷University of California, Berkeley, California 94720
- ⁸University of California, Davis, California 95616
- ⁹University of California, Los Angeles, California 90095
- ¹⁰University of California, Riverside, California 92521
- ¹¹Central China Normal University, Wuhan, Hubei 430079
- ¹²University of Illinois at Chicago, Chicago, Illinois 60607
- ¹³Creighton University, Omaha, Nebraska 68178
- ¹⁴Czech Technical University in Prague, FNSPE, Prague 115 19, Czech Republic
- ¹⁵Technische Universität Darmstadt, Darmstadt 64289, Germany
- ¹⁶ELTE Eötvös Loránd University, Budapest, Hungary H-1117
- ¹⁷Frankfurt Institute for Advanced Studies FIAS, Frankfurt 60438, Germany
- ¹⁸Fudan University, Shanghai, 200433
- ¹⁹University of Heidelberg, Heidelberg 69120, Germany
- ²⁰University of Houston, Houston, Texas 77204
- ²¹Huzhou University, Huzhou, Zhejiang 313000
- ²²Indian Institute of Science Education and Research (IISER), Berhampur 760010, India
- ²³Indian Institute of Science Education and Research (IISER) Tirupati, Tirupati 517507, India
- ²⁴Indian Institute Technology, Patna, Bihar 801106, India
- ²⁵Indiana University, Bloomington, Indiana 47408
- ²⁶Institute of Modern Physics, Chinese Academy of Sciences, Lanzhou, Gansu 730000
- ²⁷University of Jammu, Jammu 180001, India
- ²⁸Joint Institute for Nuclear Research, Dubna 141 980, Russia
- ²⁹Kent State University, Kent, Ohio 44242
- ³⁰University of Kentucky, Lexington, Kentucky 40506-0055
- ³¹Lawrence Berkeley National Laboratory, Berkeley, California 94720
- ³²Lehigh University, Bethlehem, Pennsylvania 18015
- ³³Max-Planck-Institut für Physik, Munich 80805, Germany
- ³⁴Michigan State University, East Lansing, Michigan 48824
- ³⁵National Research Nuclear University MPhI, Moscow 115409, Russia
- ³⁶National Institute of Science Education and Research, HBNI, Jatni 752050, India
- ³⁷National Cheng Kung University, Tainan 70101
- ³⁸Nuclear Physics Institute of the CAS, Rez 250 68, Czech Republic
- ³⁹Ohio State University, Columbus, Ohio 43210
- ⁴⁰Institute of Nuclear Physics PAN, Cracow 31-342, Poland
- ⁴¹Panjab University, Chandigarh 160014, India
- ⁴²Pennsylvania State University, University Park, Pennsylvania 16802
- ⁴³NRC "Kurchatov Institute", Institute of High Energy Physics, Protvino 142281, Russia
- ⁴⁴Purdue University, West Lafayette, Indiana 47907
- ⁴⁵Rice University, Houston, Texas 77251
- ⁴⁶Rutgers University, Piscataway, New Jersey 08854
- ⁴⁷Universidade de São Paulo, São Paulo, Brazil 05314-970
- ⁴⁸University of Science and Technology of China, Hefei, Anhui 230026
- ⁴⁹Shandong University, Qingdao, Shandong 266237
- ⁵⁰Shanghai Institute of Applied Physics, Chinese Academy of Sciences, Shanghai 201800
- ⁵¹Southern Connecticut State University, New Haven, Connecticut 06515
- ⁵²State University of New York, Stony Brook, New York 11794
- ⁵³Instituto de Alta Investigación, Universidad de Tarapacá, Arica 1000000, Chile
- ⁵⁴Temple University, Philadelphia, Pennsylvania 19122
- ⁵⁵Texas A&M University, College Station, Texas 77843
- ⁵⁶University of Texas, Austin, Texas 78712
- ⁵⁷Tsinghua University, Beijing 100084
- ⁵⁸University of Tsukuba, Tsukuba, Ibaraki 305-8571, Japan
- ⁵⁹Valparaiso University, Valparaiso, Indiana 46383
- ⁶⁰Variable Energy Cyclotron Centre, Kolkata 700064, India
- ⁶¹Warsaw University of Technology, Warsaw 00-661, Poland
- ⁶²Wayne State University, Detroit, Michigan 48201

We report a new measurement of the production cross section for inclusive electrons from open heavy-flavor hadron decays as a function of transverse momentum (p_T) at mid-rapidity ($|y| < 0.7$) in $p+p$ collisions at $\sqrt{s} = 200$ GeV. The result is presented for $2.5 < p_T < 10$ GeV/ c with an improved precision at high p_T with respect to the previous measurements, and thus provides a better constraint on perturbative QCD calculations. Moreover, this measurement also provides a high-precision reference for measurements of nuclear modification factors for inclusive electrons from open-charm and -bottom hadron decays in heavy-ion collisions.

I. INTRODUCTION

Ultra-relativistic heavy-ion collisions provide a unique opportunity for studying Quantum Chromodynamics (QCD) under controlled laboratory conditions. The force binding quarks together in nucleons can be screened at sufficiently high energy density, which leads to a transition from ordinary nuclear matter to a new phase, the properties of which are governed by quark and gluon degrees of freedom. This state of matter is called Quark-Gluon Plasma (QGP). It is hypothesized to have existed in the early universe, a few millionths of a second after the Big Bang [1, 2]. Experiments at the Relativistic Heavy Ion Collider (RHIC) and Large Hadron Collider (LHC) have provided strong evidence that a strongly interacting QGP is created in collisions of heavy ions at RHIC and LHC energies [3–7].

Heavy quarks are an excellent probe of the QGP. They are produced early in heavy-ion collisions, in the initial parton-parton interactions with large momentum transfers, and therefore they carry information about the system evolution [8, 9]. Heavy quarks are expected to suffer from collisional and radiative energy loss through interactions with the QGP. Measurements of heavy quark production are crucial for understanding the nature of interactions of heavy quarks with the surrounding partonic medium, and the parton energy loss mechanisms in general. The nuclear modification factor (R_{AA}) is constructed to quantify medium effects in relativistic heavy-ion collisions [10], including those from heavy-flavor energy loss. Significant suppression of the charm meson yield at large transverse momenta (p_T), resulting from the substantial energy loss of heavy quarks in the QGP, has been observed at both RHIC and LHC [11–16], indicating significant interactions between heavy quarks and the medium.

Heavy quark production in $p+p$ collisions serves as a baseline to similar measurements in heavy-ion collisions. It is predicted to be well described by perturbative QCD (pQCD) FONLL (Fixed-Order Next-to-Leading Logarithm) calculations, as the masses of the heavy quarks are much larger than the QCD scale parameter Λ_{QCD} [9]. Charmed hadron production in $p+p$ collisions has been measured by the Solenoidal Tracker at

RHIC (STAR) [17], and was found to be consistent with the upper limit of pQCD FONLL calculations. Due to a large combinatorial background, these earlier measurements have a limited p_T range ($p_T < 6$ GeV/ c). Electrons¹ from semileptonic decays of heavy-flavor hadrons (HFE) are good proxies for open heavy quarks. Although kinematic information regarding the parent heavy-flavor hadrons is incomplete, and the HFE sample is usually a mixture of electrons from both charm and beauty hadron decays, HFEs are still widely used to study heavy quark production. Moreover, data collection of high- p_T electrons can be enhanced in an experiment thanks to dedicated electron triggers. The inclusive HFE production in $p+p$ collisions at $\sqrt{s} = 200$ GeV has been studied by STAR [18] and PHENIX [19]. These earlier results are also consistent with pQCD FONLL calculations, however they have large uncertainties at high p_T .

In this paper, we report a new measurement of the inclusive HFE cross section at mid-rapidity ($|y| < 0.7$) in $p+p$ collisions at $\sqrt{s} = 200$ GeV. The cross section for inclusive HFE as a function of p_T ($2.5 < p_T < 10$ GeV/ c) is obtained with higher precision at high p_T than the previously published results [18, 19]. The paper is organized as follows. In Sec. II, components of the STAR detector relevant to this analysis are briefly discussed. Section III is dedicated to the details of the data analysis of inclusive HFE production. Finally, the results are reported and compared with published results and model calculations in Sec. IV.

II. EXPERIMENTAL SETUP

A. Detector

STAR [20] is a multi-purpose detector with large acceptance at RHIC. In this analysis, three main STAR subsystems are used: the Time Projection Chamber (TPC) [21], the Barrel Electromagnetic Calorimeter (BEMC) [22], and the Beam-Beam Counters (BBC) [23]. The STAR TPC is a gas-filled detector providing tracking of charged particles with pseudorapidity $|\eta| < 1$ and full azimuthal angle range. It is used for momentum

* Deceased

¹ Unless specified otherwise, electrons referred here include both electrons and positrons and results are presented as $\frac{e^+ + e^-}{2}$.

measurement and particle identification via energy loss (dE/dx) for charged particles with $p_T > 0.2$ GeV/ c . The STAR BEMC is a lead-scintillator sampling calorimeter surrounding the TPC with a depth of 21 radiation lengths, which covers the full azimuth and $|\eta| < 1$. The BEMC is segmented into 4800 projective towers, each with size of 0.05×0.05 in $\phi \times \eta$. It is used for electron identification and as a fast trigger detector for high- p_T electrons. The STAR BBC, covering $3.3 < |\eta| < 5.0$, is located on both sides of the center of the detector at a distance of 3.75 m. Each BBC is made up of 18 hexagonal scintillator tiles. Signals in both BBCs form a prompt coincidence to provide a minimum bias trigger.

B. Triggers and Datasets

The measurement reported here of HFE production in $p+p$ collisions at $\sqrt{s} = 200$ GeV utilizes data recorded by the STAR experiment in 2012 that satisfy the High Tower (HT) triggers in addition to the BBC minimum bias trigger condition. HT triggers require the transverse energy (E_T) deposition in at least one single BEMC tower to pass a given Analog to Digital Converter (ADC) threshold. The tower ADC value is proportional to the E_T deposited by particles. Events used in this analysis are from two HT triggers with E_T thresholds of 2.6 GeV (HT0) and 4.2 GeV (HT2), which correspond to 1.4 and 23.5 pb^{-1} integrated luminosities, respectively. For HT triggered events used in this analysis, particle tracks in the TPC are projected onto the BEMC tower plane, and only those electron candidates whose projected trajectory can be associated to a BEMC cluster that satisfies the HT trigger are selected. The results presented in this paper combine HT0 events for $p_T < 4.5$ GeV/ c and HT2 for $p_T \geq 4.5$ GeV/ c .

III. DATA ANALYSIS FOR INCLUSIVE HFE PRODUCTION

A. Analysis principles

Three principal steps are carried out to measure HFE production at STAR:

1. identification, purity and efficiency correction of inclusive electrons (INE),
2. identification and efficiency correction of the photonic electrons (PHE), and subtraction of PHE from the INE sample,
3. subtraction of remaining background sources called hadron decayed electrons (HDE), including di-electron decays of light vector mesons (ρ , ω , ϕ), quarkonium decays (J/ψ , Υ), Drell-Yan processes, and kaon semi-leptonic decays (K_{e3}).

The first two steps can be summarized by

$$N_{\text{NPE}} = \frac{N_{\text{INE}} \times P_e - N_{\text{PHE}}/\epsilon_{\text{PHE}}}{\epsilon_{\text{total}}}, \quad (1)$$

where N_{NPE} is the non-photonic electron (NPE) yield, N_{INE} is the inclusive electron candidate yield, P_e is the purity of the electron sample, N_{PHE} is the photonic electron yield, ϵ_{PHE} is the photonic electron identification efficiency, and ϵ_{total} is the overall efficiency for trigger, track reconstruction and electron identification.

In the first step, electron candidates are identified using combined information from the TPC and BEMC, and a purity correction to account statistically for hadron contamination is applied to obtain the inclusive electron sample ($N_{\text{INE}} \times P_e$). In the second step, the yield of photonic electrons, which is the main source of background in this analysis, is calculated. It consists of electrons from photon conversion in the detector material and Dalitz decays of π^0 and η mesons ($\pi^0 \rightarrow \gamma e^+ e^-$, $\eta \rightarrow \gamma e^+ e^-$). The contribution of photonic electrons is statistically identified by reconstructing the di-electron mass ($M_{e^+e^-}$) spectrum. The observed photonic electron yield is corrected for photonic electron identification efficiency ($N_{\text{PHE}}/\epsilon_{\text{PHE}}$) and subtracted from the inclusive electron sample. The remaining electrons in the inclusive electron sample are then corrected for single electron tracking, trigger, and identification efficiencies to estimate the non-photonic electron yield. In the last step, the HDE background is subtracted. After the subtraction, the remaining electron sample is from open charm and bottom hadron decays.

B. Event selection and electron identification

During data processing, the event vertex is reconstructed offline in 3 dimensions, based on charged particle trajectories in the TPC, and it is called the primary vertex. In addition, tracks are matched to hits in either the BEMC or Time-of-Flight [24] detectors in vertex selection to suppress pileup. Only events with primary vertices located within ± 35 cm from the geometrical center of the TPC along the beam line direction and within 2 cm in the radial direction are selected in the analysis to ensure a uniform TPC acceptance.

A set of selection criteria is applied to ensure a high quality sample of tracks in the analysis. The number of points measured in the TPC (TPC hits) of a track is required to be at least 20 and also to be higher than 52% of the maximum possible number of TPC hits, which accounts, *e.g.*, for inactive electronic channels, to ensure good tracking and to avoid one track splitting into two tracks. At least 15 of these TPC hits must be used to measure the charged particle ionizing energy loss in the TPC gas to ensure a good dE/dx resolution. The distance-of-closest-approach (DCA) between a track trajectory in the TPC and the primary vertex is required to be less than 1.5 cm to enhance the probability of finding

electron candidates originating from the primary vertex. Additional selections are applied to minimize photonic electron background from photon conversions in detector materials. Tracks are required to have $|\eta| < 0.7$ to avoid the beam pipe support structure. Also, to suppress photon conversion in the TPC gas, we require at least one hit within the first three TPC pad rows.

Electrons are identified using dE/dx in the TPC and energy deposited in the BEMC towers. First, the BEMC clusters are associated with the TPC tracks by projecting track trajectories onto the BEMC tower plane, and electron candidates are required to have the momentum-to-energy ratio (p/E) from 0.3 to 1.5 [25], where energy is that of the most energetic tower in a BEMC cluster and momentum is measured by the TPC. Second, tracks with $-0.5 < n\sigma_e < 3$ are selected, where $n\sigma_e$ represents a standardized energy loss expected for electrons. The $n\sigma_e$ is defined as $n\sigma_e = \ln((dE/dx_{mea})/(dE/dx_{th}))/\sigma_{dE/dx}$, where dE/dx_{mea} is the measured value, dE/dx_{th} is the theoretical value for electrons and $\sigma_{dE/dx}$ is the experimental dE/dx resolution. Electron candidates that pass all the aforementioned selection criteria are called the inclusive electrons. They are composed primarily of electrons, including HFE, PHE, and HDE sources, but also contain some hadron contamination.

C. Electron Purity

The electron purity of the inclusive electron sample is estimated by a constrained fit to the $n\sigma_e$ distribution of inclusive electron candidates in each p_T bin, prior to the $n\sigma_e$ selection being applied. Three Gaussian functions representing the distributions of π^\pm , $K^\pm + p(\bar{p})$, and e^\pm are summed together to fit the $n\sigma_e$ distribution. The following constraints on the Gaussian representing electrons are obtained based on the $n\sigma_e$ distribution for a selected sample of pure electrons (photonic electrons with a tight invariant mass cut $M_{e^+e^-} < 0.1$ GeV/ c^2 obtained as described in Sec. III D). For each p_T bin, we fit the pure electron $n\sigma_e$ distribution with a single Gaussian and the obtained mean and width are used to constrain the electron Gaussian in the three-Gaussian fit of the inclusive electron candidates. The $n\sigma_e$ distributions for hadrons are also expected to follow Gaussian distributions. The initial mean $n\sigma_e$ values in the fit are obtained from theoretical Bichsel function [26] calculations and the initial widths are set to be one. Figure 1 (a) shows an example of the three-Gaussian fit to the inclusive electron candidates at $4.5 < p_T < 5.0$ GeV/ c . The $n\sigma_e$ distribution with the three-Gaussian fit provides enough information to calculate the electron purity. The purity is obtained by taking the ratio of the integral of the electron fit function to that of the overall fit function in the selected $n\sigma_e$ range ($-0.5 < n\sigma_e < 3$). Figure 1 (b) shows the purity of the inclusive electron sample as a function of p_T with statistical and systematic uncertainties described in Sec. IV.

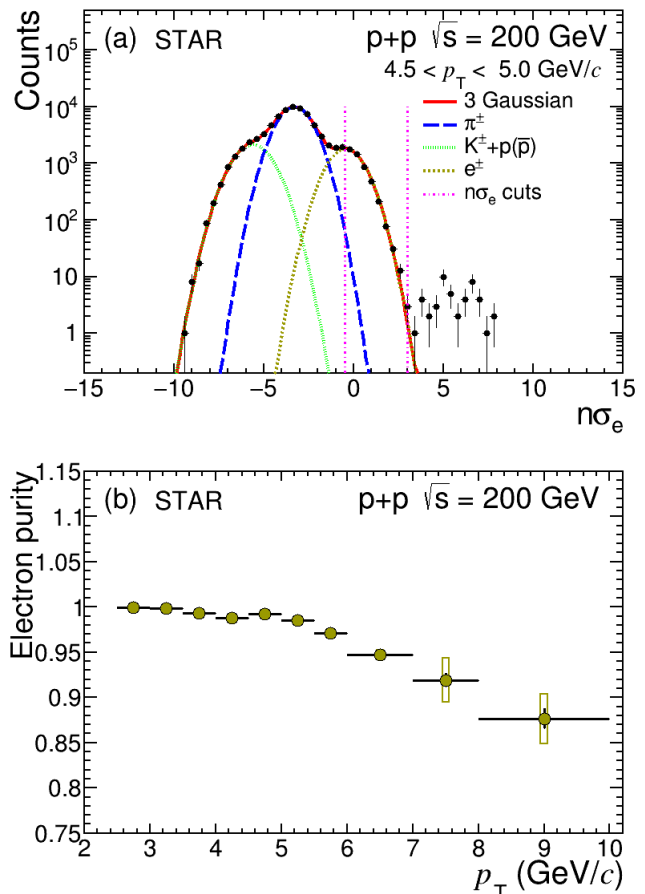


FIG. 1. (a) Example of $n\sigma_e$ distribution (black circles) with three-Gaussian fit (solid red curve) at $4.5 < p_T < 5.0$ GeV/ c in $p+p$ collisions at $\sqrt{s} = 200$ GeV. Gaussian functions (dotted curves in various colors) represent fits for different particle species. The dotted pink vertical lines indicate the $-0.5 < n\sigma_e < 3$ range used for electron selection. The small bump at $4 < n\sigma_e < 10$ is from the merging of two tracks [27]. (b) Electron purity as a function of p_T in $p+p$ collisions at $\sqrt{s} = 200$ GeV. The vertical bars represent statistical uncertainties while the boxes represent systematic uncertainties.

D. Photonic electron subtraction

Photonic electrons come from 2-body γ conversions ($\gamma \rightarrow e^+e^-$) and 3-body Dalitz decays of π^0 and η mesons ($\pi^0/\eta \rightarrow e^+e^-\gamma$). Each electron among the inclusive electron candidates (tagged electron) is paired with an oppositely charged track (partner electron) in the TPC in the same event to reconstruct their photonic parent, γ , π^0 , or η . Such pairs are called unlike-sign (US) pairs. Unless specified otherwise, p_T referred for electron pairs is that of the tagged electrons. A looser set of identification and quality cuts ($|\eta| < 1$, at least 15 TPC hits and $p_T > 0.3$ GeV/ c) are applied to select partner electrons, in order to enhance the chance of finding photonic electrons. No $n\sigma_e$ and BEMC p/E cuts are applied to the partner electrons. In addition, a maximum 1.0 cm DCA

between two helical-shaped electron tracks is required to ensure partner tracks have the same origin. In the STAR detector, the primary momentum of a track is calculated with the assumption that every track originates from the primary vertex and the primary vertex should be part of the track trajectory. However, since photon conversions mostly take place in detector materials, typically away from the primary collision vertex, such a primary vertex requirement would thus introduce bias in the reconstruction of photonic parents. Instead, the so-called global track momentum, which is calculated without including the primary vertex as part of the track trajectory, is used in the photonic reconstruction.

In order to account for the combinatorial background present in the selected e^+e^- pair sample, tagged electrons are also paired with same-charge partner electrons (like-sign (LS) pairs) in the same event. Figure 2 (a) shows an example of invariant mass distributions for all e^+e^- pairs, combinatorial background and photonic electrons at $4.5 < p_T < 5.0$ GeV/c. The photonic parents are selected as pairs with $M_{e^+e^-} < 0.24$ GeV/c² to take into account the broadening of $M_{e^+e^-}$ due to the worsening of the momentum resolution at higher p_T , and this mass cut has an efficiency changing from 99% to 94% with increasing p_T . The photonic electron yield is calculated as $N_{\text{PHE}} = (N_{\text{US}} - N_{\text{LS}})$, where N_{US} and N_{LS} are the number of unlike-sign and like-sign tagged electrons after the mass selection, respectively.

The photonic electron identification efficiency, ε_{PHE} , is calculated from a full GEANT [28] simulation of the STAR detector that includes π^0 , η decays and γ conversions, embedded into real events. The combined events then go through the same reconstruction and analysis software chain as the real data. Such events are called embedded events. The published η [29–32] and charged and neutral pion spectra [29, 33, 34] are used as the inputs for η and π^0 simulations. The input γ p_T spectrum is a combination of measured direct γ by the PHENIX experiment [35–37] and simulated $\pi^0 \rightarrow \gamma\gamma/e^+e^-\gamma$ and $\eta \rightarrow \gamma\gamma/e^+e^-\gamma$ obtained through PYTHIA 6.419 [38] decays with default settings from the aforementioned π^0 and η spectra as the inputs. The rapidity distributions of π^0 and η used in PYTHIA decays are parameterized with a Gaussian-like function $\cosh^{-2}\left(\frac{3y}{4\sigma(1-y^2/(2\sqrt{s}/m))}\right)$, where $\sigma = \sqrt{\ln(\sqrt{s}/(2m_N))}$, \sqrt{s} is a nucleon-nucleon center of mass energy, m is the particle mass, and m_N is the nucleon mass [39–41]. All these photonic sources are then combined together, according to their relative total cross sections. Figure 2 (b) shows ε_{PHE} as a function of p_T for γ conversion and two types of Dalitz decays in $p+p$ collisions. The ε_{PHE} are similar for all components. The overall ε_{PHE} , which starts from about 40% at low p_T and increases with p_T up to about 60% at $p_T \sim 10$ GeV/c, is also shown in Fig. 2 (b), along with a fit function $A/(e^{-(p_T-p_0)/p_1} + 1) + C$, where A , p_0 , p_1 , and C are free parameters.

After statistical subtraction of hadron contaminations

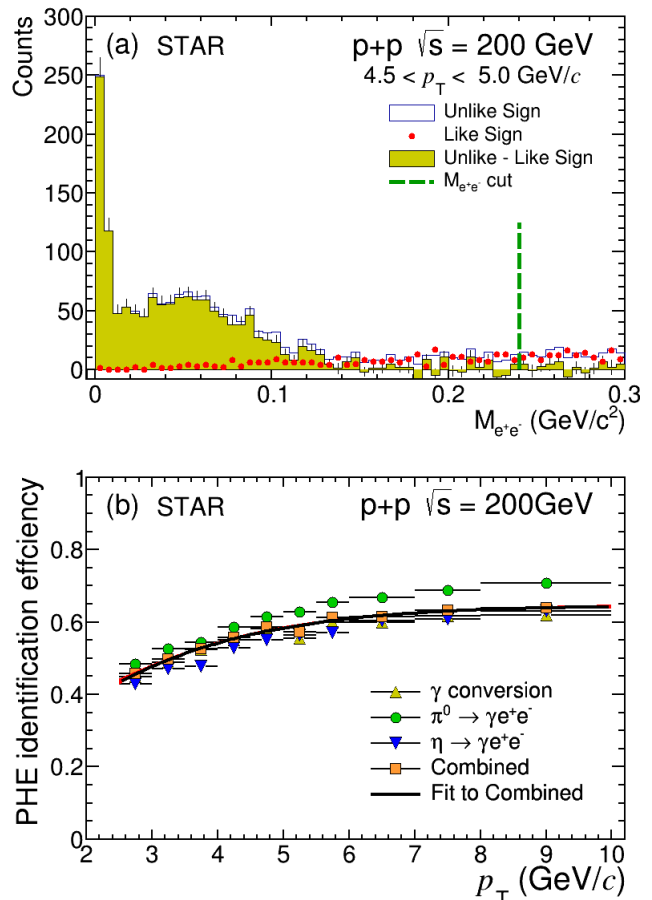


FIG. 2. (a) Example of invariant mass distribution for electron pairs at electron $4.5 < p_T < 5.0$ GeV/c in $p+p$ collisions at $\sqrt{s} = 200$ GeV. The blue histogram labelled “Unlike Sign” are the e^+e^- pairs, the red circles labelled “Like Sign” represent the combinatorial background and the difference of these two is the photonic electrons, shown as the yellow histogram labelled “Unlike-Like Sign”. The dotted green vertical line indicates the photonic electron selection; (b) Combined photonic electron identification efficiency (orange squares) together with a fit (black curve) and parameterization uncertainty (red band which is hard to see due to the small width), and individual photonic electron identification efficiencies: photon conversion (yellow up triangles), π^0 Dalitz decay (green circles), and η Dalitz decay (blue down triangles) as a function of p_T in $p+p$ collisions at $\sqrt{s} = 200$ GeV.

and photonic electrons, the remaining electrons are the non-photonic ones. Figure 3 shows the ratio of non-photonic electron signal and photonic electron background as a function of p_T .

E. Track reconstruction and electron identification efficiency

Before removing the HDE background, the non-photonic electron sample needs to be corrected for over-

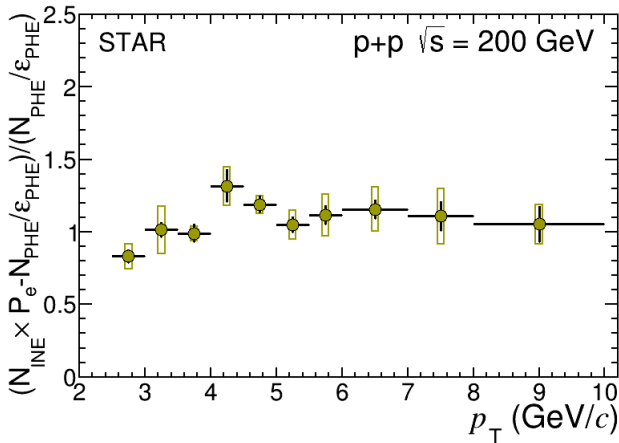


FIG. 3. Signal-to-background ratio as a function of p_T , where the signals are non-photonic electrons ($N_{\text{INE}} \times P_e - N_{\text{PHE}}/\epsilon_{\text{PHE}}$ in Eq. (1)) and the backgrounds are photonic electrons ($N_{\text{PHE}}/\epsilon_{\text{PHE}}$ in Eq. (1)), in $p+p$ collisions at $\sqrt{s} = 200$ GeV. The vertical bars represent statistical uncertainties while the boxes represent systematic uncertainties (details in Sec. IV).

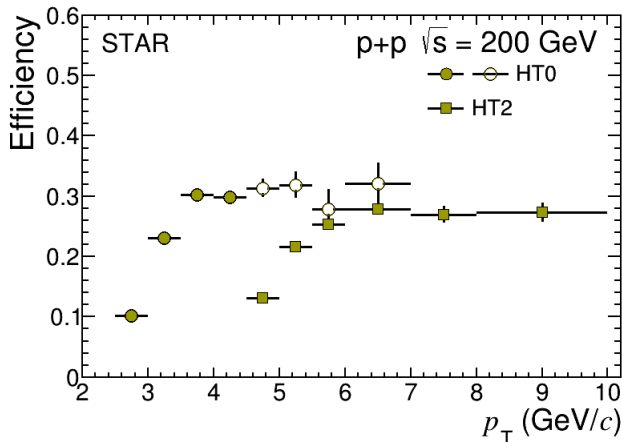


FIG. 4. Electron detection efficiency as a function of p_T in $p+p$ collisions at $\sqrt{s} = 200$ GeV. The circles and squares are the efficiency for HT0- and HT2-triggered electrons, respectively. The vertical bars represent uncertainties. The solid points are used to correct the non-photonic electron yield.

all efficiency of trigger, track reconstruction and electron identification. The combined detector acceptance and tracking efficiency is studied based on the embedded events of single electrons. The $n\sigma_e$ cut efficiency is calculated based on the Gaussian fit to the pure electron sample, as described in Sec. III C. The BEMC particle identification (PID) and trigger efficiencies are studied in embedded events with GEANT simulated BEMC responses to electrons. The BEMC PID efficiency is evaluated by taking the ratio of electrons with and without the BEMC selection. The trigger efficiency is obtained by requiring the offline ADC value of the most energetic tower

in a BEMC cluster, which was matched to an electron track, to be larger than the threshold. Figure 4 shows the overall single electron efficiency as a function of p_T for HT0- and HT2-triggered electrons. The efficiency is about 10–30% and increases with p_T . The solid points are used to correct the non-photonic electrons.

F. Hadron decayed electron background

Electrons from di-electron decays of light vector mesons (ρ , ω , ϕ), heavy quarkonium decays (J/ψ , Υ), Drell-Yan processes, and kaon semi-leptonic decays (K_{e3}) are additional sources of background which should be subtracted to study the semileptonic decays of open heavy flavors.

Inclusive J/ψ spectra have been measured in $p+p$ collisions at mid-rapidity by both the STAR [42] and PHENIX [43] collaborations, and the combined J/ψ p_T spectra are parametrized with the Tsallis statistics [44–46]. The J/ψ rapidity distribution is from PYTHIA [47]. Since decayed electrons from non-prompt J/ψ are one of the components of bottom-decayed electrons, the FONLL+CEM calculations [9, 48] are used to remove the non-prompt J/ψ contribution from the inclusive J/ψ sample. J/ψ particles are generated according to the parameterized p_T spectrum, after removing the non-prompt J/ψ contribution, and EvtGen [49] is utilized to describe their decay to electrons. In this process, we assume that J/ψ is unpolarized, which is consistent with the STAR measurement [50]. The J/ψ decayed electron cross section is represented by the dot-dashed line in Fig. 5.

The Υ decayed electron contribution is estimated in a similar way as that for the J/ψ except the input Υ spectrum and rapidity. The p_T spectra of Υ states are parameterized with the following function: $f = C \times \frac{p_T}{e^{p_T/T} + 1}$, where the values of the T and C parameters are taken from Ref. [51]. The rapidity distribution of Υ is parametrized with the Gaussian-like function mentioned in Sec. III D. The cross section of the electrons from Υ decay is represented by the dotted line in Fig. 5.

The vector meson spectra are obtained by m_T ($\sqrt{p_T^2 + m^2}$) scaling of the π^0 p_T -shape (replacing the p_T with $\sqrt{p_T^2 + m_m^2 - m_{\pi^0}^2}$ in the same fit function, here m_m is the mass of the vector meson) and then matching the ratio of meson over π^0 to the measured values at high p_T (ρ/π^0 from the Tsallis fit in the STAR published di-electron measurement [52], and $\omega/\pi^0 = 0.90 \pm 0.06$ and $\phi/\pi^0 = 0.25 \pm 0.08$ from Ref. [19]). Their rapidity distributions are also obtained from calculation of a Gaussian-like function. EvtGen is used to decay ω and ϕ , and PYTHIA 6.419 with default settings is used to decay ρ (EvtGen doesn't provide the electron decay channel for ρ). The contribution from vector meson decays is represented by the long dashed line in Fig. 5. We include the following decay channels $\rho \rightarrow e^+e^-$, $\omega \rightarrow e^+e^-$, $\omega \rightarrow \pi^0 e^+e^-$, $\phi \rightarrow e^+e^-$, and $\phi \rightarrow \eta e^+e^-$ in the calcula-

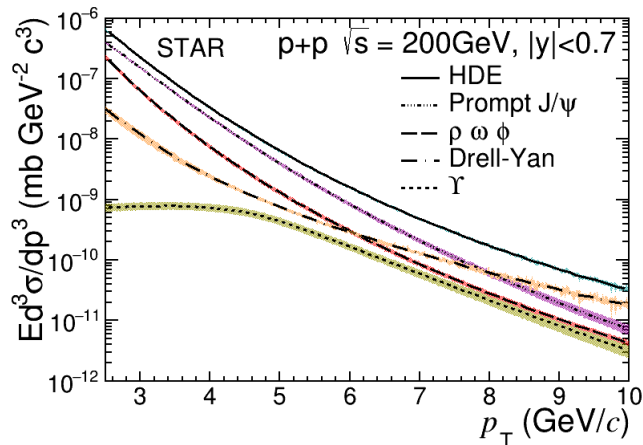


FIG. 5. Invariant cross section of the electrons from decays of prompt J/ψ (dot-dashed line), Υ (dotted line), Drell-Yan (long dash-dotted line), light vector mesons (long dashed line) and the overall HDE contributions (solid line) in $p+p$ collisions at $\sqrt{s} = 200$ GeV. The bands represent systematic uncertainties (details in Sec. IV).

tion.

The Drell-Yan contribution is estimated by the PYTHIA simulation, which has the same settings as the PHENIX published Drell-Yan result [53], and is shown as the long dash-dotted line in Fig. 5. STAR simulation studies find that the K_{e3} contribution is less than 1% at $p_T > 2$ GeV/c in $p+p$ collisions at $\sqrt{s} = 200$ GeV [54] and thus can be neglected. The overall HDE contributions represented by the solid line in Fig. 5 are subtracted from the non-photonic electron sample, and the remaining electrons are HFE reported in Sec. IV.

IV. RESULTS

The HFE cross section in $p+p$ collisions is obtained as:

$$E \frac{d^3\sigma}{dp^3}(\text{HFE}) = \frac{1}{2} \frac{1}{L} \frac{N_{\text{NPE}}}{2\pi p_T \Delta p_T \Delta y} - E \frac{d^3\sigma}{dp^3}(\text{HDE}), \quad (2)$$

where L is the integrated luminosity, p_T is the weighted average of the bin, Δp_T and Δy are the p_T and rapidity intervals, respectively. $L = \frac{N_{\text{events}}}{\sigma_{\text{NSD}}}$, where N_{events} is the equivalent number of minimum bias events of the collected data and σ_{NSD} is the non-singly diffractive cross section, which is obtained by $\sigma_{\text{inel}}^{pp}/R_\sigma$. The $p+p$ inelastic cross section $\sigma_{\text{inel}}^{pp} = 42$ mb, and the factor $R_\sigma = 1.4$ [17].

The total systematic uncertainty is obtained as the square root of the quadratic sum of the individual systematic uncertainties. The uncertainties from the NPE raw yield extraction and efficiency are estimated by varying the corresponding selection criteria, *e.g.* track quality and electron identification cuts, simultaneously in data and embedding. The uncertainty on electron purity is estimated based on the mean and width uncertainties of

TABLE I. Summary of systematic uncertainties, in percentage, for the HFE cross section.

Source	Uncertainty
NPE raw yield extraction and efficiency	2.0-12.5%
Electron purity extraction	0.1-7.3%
PHE reconstruction efficiency	2.0-4.4%
$n\sigma_e$ cut efficiency	1.9-7.3%
BBC trigger and vertex reconstruction efficiencies	4.9-5.2%
HDE contribution	0.7-1.4%
Luminosity	8%

the Gaussian fit to the pure electron $n\sigma_e$ distribution. The uncertainty of PHE identification efficiency stems from the uncertainty on the parameterization of PHE reconstruction efficiency, on the parameterization of π^0 and η spectra, on the branching ratio for electron from π^0 and η decays, and on the tracking efficiency of partner electrons. The uncertainty of the $n\sigma_e$ cut efficiency is taken from that of the Gaussian fit to the pure electron sample. The uncertainty of the HDE contribution includes those from J/ψ , Υ , vector meson, and Drell-Yan contributions. The parameterization uncertainty from inclusive J/ψ and uncertainty from FONLL+CEM calculations of the non-prompt J/ψ contribution to the inclusive J/ψ are taken as the uncertainty on the estimation of the prompt J/ψ decayed electron cross section. The uncertainties from the T value and Υ cross section are taken as the systematic uncertainty on the estimation of the Υ decayed electron cross section. The parameterization uncertainty from π^0 and the ratio of meson over π^0 uncertainties are taken as the systematic uncertainty of di-electron decays of light vector mesons. The uncertainty from the Drell-Yan contribution is estimated by using the same method as in the PHENIX published Drell-Yan result [53]. The uncertainty from the BBC trigger and vertex reconstruction efficiencies amounts to 4.9-5.2% by the multiplicity difference in data and simulation, the difference in the simulation versions (PYTHIA 6 vs PYTHIA 8), and the different parameter settings in the simulation (STAR heavy flavor tune [17] vs STAR heavy flavor tune plus 4CX one [38]). The global uncertainty from the luminosity determination is 8% [17]. Table I summarizes the size of the uncertainties arising from different sources.

In order to compare with the published STAR [18] and PHENIX [19] results, where light vector meson decayed electrons were subtracted instead of HDE, we first subtract the light vector meson (ρ , ω , ϕ) contribution from the non-photonic electrons:

$$E \frac{d^3\sigma}{dp^3}(\text{NPE}_{\text{woLVMDE}}) = \frac{1}{2} \frac{1}{L} \frac{N_{\text{NPE}}}{2\pi p_T \Delta p_T \Delta y} - E \frac{d^3\sigma}{dp^3}(\text{LVMDE}), \quad (3)$$

where $E \frac{d^3\sigma}{dp^3}(\text{LVMDE})$ is the cross section of electrons from light vector meson decays. The result is shown in Fig. 6 (a), together with the previously published results. A combined power-law fit to the PHENIX data and the

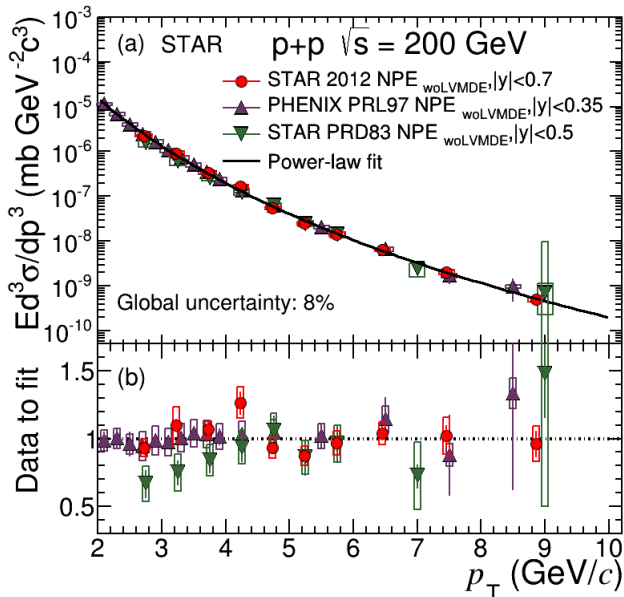


FIG. 6. (a) The NPE cross section after subtracting the light vector meson contribution at STAR in $p+p$ collisions at $\sqrt{s} = 200$ GeV from 2012 (filled circles) along with published STAR data from 2005 and 2008 (filled down triangles) [18], published PHENIX data from 2005 (filled up triangles) [19] and power-law fit (curve). (b) Ratio of data over power-law fit. The vertical bars and the boxes represent statistical and systematic uncertainties, respectively.

result presented in this paper is also shown in Fig. 6 (a). A comparison of results is plotted as a ratio to the power-law fit in Fig. 6 (b). Overall, there is a good agreement among these results within their uncertainties. The new result is measured with significantly improved precision relative to the previous measurements, especially at high p_T . Figure 7 (a) shows the measured HFE cross section for $p+p$ collisions at $\sqrt{s} = 200$ GeV, along with the FONLL calculations. The ratio of HFE data to the FONLL calculations is shown in Fig. 7 (b). The result reported in this paper is qualitatively consistent with the upper limit of the FONLL prediction within the uncertainty.

V. SUMMARY

The measurement of the cross section for production of electrons from open-charm and open-bottom hadron decays for $2.5 < p_T < 10$ GeV/ c in $p+p$ collisions at $\sqrt{s} = 200$ GeV is reported. The result before subtracting the J/ψ , Υ , and Drell-Yan contribution is consistent with the STAR and PHENIX published results, and measured with significantly improved precision relative to the previous measurements. The hadron decayed electron subtracted result is qualitatively consistent with the FONLL upper limit within the uncertainty and provides further constraints on theoretical calculations. Further-

more, this result provides a more precise reference for nuclear modification factor R_{AA} measurements in heavy-ion collisions and further study on isolation of the charm and bottom contributions in HFE in $p+p$ collisions [55].

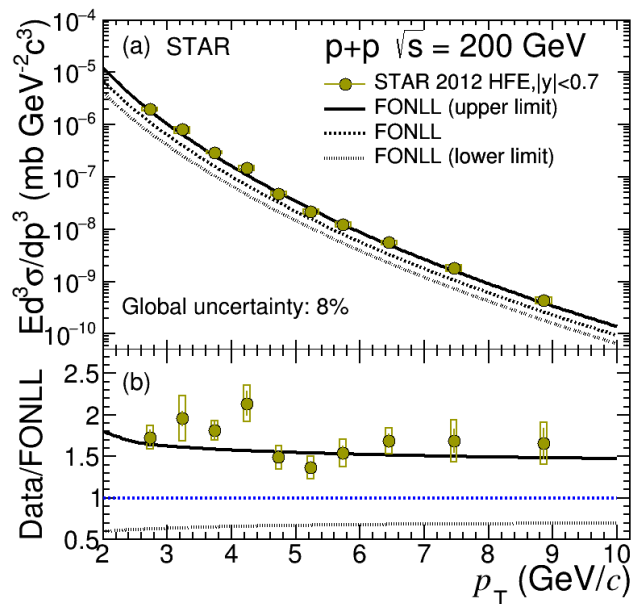


FIG. 7. (a) The HFE cross section at STAR in $p+p$ collisions at $\sqrt{s} = 200$ GeV from 2012 (filled circles) and the FONLL calculations (curves). (b) Ratio of data over FONLL calculations. The vertical bars and the boxes represent statistical and systematic uncertainties, respectively.

VI. ACKNOWLEDGEMENT

We thank the RHIC Operations Group and RCF at BNL, the NERSC Center at LBNL, and the Open Science Grid consortium for providing resources and support. This work was supported in part by the Office of Nuclear Physics within the U.S. DOE Office of Science, the U.S. National Science Foundation, the Ministry of Education and Science of the Russian Federation, National Natural Science Foundation of China, Chinese Academy of Science, the Ministry of Science and Technology of China and the Chinese Ministry of Education, the Higher Education Sprout Project by Ministry of Education at NCKU, the National Research Foundation of Korea, Czech Science Foundation and Ministry of Education, Youth and Sports of the Czech Republic, Hungarian National Research, Development and Innovation Office, New National Excellency Programme of the Hungarian Ministry of Human Capacities, Department of Atomic Energy and Department of Science and Technology of the Government of India, the National Science Centre of Poland, the Ministry of Science, Education and Sports of the Republic of Croatia, RosAtom of Russia and German Bundesministerium für Bildung, Wissenschaft,

Forschung and Technologie (BMBF), Helmholtz Association, Ministry of Education, Culture, Sports, Science,

and Technology (MEXT) and Japan Society for the Promotion of Science (JSPS).

-
- [1] J. Ellis, From Little Bangs to the Big Bang, *J. Phys.: Conf. Ser.* **50**, 002 (2006).
- [2] P. Braun-Munzinger and J. Stachel, The quest for the quark-gluon plasma, *Nature* **448**, 302 (2007).
- [3] I. Arsene *et al.* (BRAHMS Collaboration), Quark-gluon plasma and color glass condensate at RHIC? The perspective from the BRAHMS experiment, *Nucl. Phys. A* **757**, 1 (2005).
- [4] J. Adams *et al.* (STAR Collaboration), Experimental and theoretical challenges in the search for the quark-gluon plasma: The STAR Collaboration's critical assessment of the evidence from RHIC collisions, *Nucl. Phys. A* **757**, 102 (2005).
- [5] K. Adcox *et al.* (PHENIX Collaboration), Formation of dense partonic matter in relativistic nucleus-nucleus collisions at RHIC: Experimental evaluation by the PHENIX Collaboration, *Nucl. Phys. A* **757**, 184 (2005).
- [6] J. Schukraft, Heavy ion physics at the Large Hadron Collider: what is new? What is next?, *Phys. Scr.* **T158**, 014003 (2013).
- [7] P. Braun-Munzinger, V. Koch, T. Schäfer, and J. Stachel, Properties of hot and dense matter from relativistic heavy ion collisions, *Phys. Rept.* **621**, 76 (2016).
- [8] Z. Lin and M. Gyulassy, Open charm as a probe of pre-equilibrium dynamics in nuclear collisions, *Phys. Rev. C* **51**, 2177 (1995), Erratum: *Phys. Rev. C* **52**, 440 (1995).
- [9] M. Cacciari, P. Nason, and R. Vogt, QCD Predictions for Charm and Bottom Quark Production at RHIC, *Phys. Rev. Lett.* **95**, 122001 (2005).
- [10] C. Adler *et al.* (STAR Collaboration), Centrality Dependence of High- p_T Hadron Suppression in Au + Au Collisions at $\sqrt{s_{NN}} = 130$ GeV, *Phys. Rev. Lett.* **89**, 202301 (2002).
- [11] Z.-B. Tang, W.-M. Zha, and Y.-F. Zhang, An experimental review of open heavy flavor and quarkonium production at RHIC, *NUCL SCI TECH* **31**, 81 (2020).
- [12] X. Luo, S. Shi, N. Xu, and Y. Zhang, A Study of the Properties of the QCD Phase Diagram in High-Energy Nuclear Collisions, *Particles* **3**, 278 (2020).
- [13] J. Adam *et al.* (STAR Collaboration), Centrality and transverse momentum dependence of D^0 -meson production at mid-rapidity in Au + Au collisions at $\sqrt{s_{NN}} = 200$ GeV, *Phys. Rev. C* **99**, 034908 (2019).
- [14] B. Abelev *et al.* (ALICE Collaboration), Suppression of high transverse momentum D mesons in central Pb-Pb collisions at $\sqrt{s_{NN}} = 2.76$ TeV, *JHEP* **2012** (09), 112.
- [15] J. Adam *et al.* (ALICE Collaboration), Transverse momentum dependence of D-meson production in Pb-Pb collisions at $\sqrt{s_{NN}} = 2.76$ TeV, *JHEP* **2016** (03), 81.
- [16] A. Sirunyan *et al.* (CMS Collaboration), Nuclear modification factor of D^0 mesons in PbPb collisions at $\sqrt{s_{NN}} = 5.02$ TeV, *Phys. Lett. B* **782**, 474 (2018).
- [17] L. Adamczyk *et al.* (STAR Collaboration), Measurements of D^0 and D^* production in $p+p$ collisions at $\sqrt{s}=200$ GeV, *Phys. Rev. D* **86**, 072013 (2012).
- [18] H. Agakishiev *et al.* (STAR Collaboration), High p_T non-photonic electron production in $p + p$ collisions at $\sqrt{s} = 200$ GeV, *Phys. Rev. D* **83**, 052006 (2011).
- [19] A. Adare *et al.* (PHENIX Collaboration), Measurement of High- p_T Single Electrons from Heavy-Flavor Decays in $p + p$ Collisions at $\sqrt{s} = 200$ GeV, *Phys. Rev. Lett.* **97**, 252002 (2006).
- [20] K. Ackermann *et al.* (STAR Collaboration), STAR detector overview, *Nucl. Instrum. Meth. A* **499**, 624 (2003).
- [21] M. Anderson *et al.*, The STAR time projection chamber: a unique tool for studying high multiplicity events at RHIC, *Nucl. Instrum. Meth. A* **499**, 659 (2003).
- [22] M. Beddo *et al.*, The STAR Barrel Electromagnetic Calorimeter, *Nucl. Instrum. Meth. A* **499**, 725 (2003).
- [23] C. A. Whitten Jr., The Beam-Beam Counter: A Local Polarimeter at STAR, in *AIP Conference Proceedings*, Vol. 980 (2008) p. 390.
- [24] B. Bonner *et al.*, A single Time-of-Flight tray based on multigap resistive plate chambers for the STAR experiment at RHIC, *Nucl. Instrum. Meth. A* **508**, 181 (2003).
- [25] Z. Tang, J/ψ production at high transverse momentum in $p+p$ and $A+A$ collisions, Ph.D. thesis, University of Science and Technology of China (2009).
- [26] H. Bichsel, A method to improve tracking and particle identification in TPCs and silicon detectors, *Nucl. Instrum. Meth. A* **562**, 154 (2006).
- [27] L. Adamczyk *et al.* (STAR Collaboration), Measurements of dielectron production in Au + Au collisions at $\sqrt{s_{NN}} = 200$ GeV from the STAR experiment, *Phys. Rev. C* **92**, 024912 (2015).
- [28] R. Brun, F. Bruyant, M. Maire, A. McPherson, and P. Zancarini, GEANT3, CERN-DD-EE-84-1 (1987).
- [29] S. S. Adler *et al.* (PHENIX Collaboration), Centrality Dependence of π^0 and η Production at Large Transverse Momentum in $\sqrt{s_{NN}} = 200$ GeV $d + Au$ Collisions, *Phys. Rev. Lett.* **98**, 172302 (2007).
- [30] A. Adare *et al.* (PHENIX Collaboration), Cross section and double helicity asymmetry for η mesons and their comparison to π^0 production in $p + p$ collisions at $\sqrt{s} = 200$ GeV, *Phys. Rev. D* **83**, 032001 (2011).
- [31] B. I. Abelev *et al.* (STAR Collaboration), Inclusive π^0 , η , and direct photon production at high transverse momentum in $p + p$ and $d + Au$ collisions at $\sqrt{s_{NN}} = 200$ GeV, *Phys. Rev. C* **81**, 064904 (2010).
- [32] S. S. Adler *et al.* (PHENIX Collaboration), High transverse momentum η meson production in $p + p$, $d + Au$, and $Au + Au$ collisions at $\sqrt{s_{NN}} = 200$ GeV, *Phys. Rev. C* **75**, 024909 (2007).
- [33] A. Adare *et al.* (PHENIX Collaboration), Inclusive cross section and double helicity asymmetry for π^0 production in $p + p$ collisions at $\sqrt{s} = 200$ GeV: Implications for the polarized gluon distribution in the proton, *Phys. Rev. D* **76**, 051106 (2007).
- [34] S. S. Adler *et al.* (PHENIX Collaboration), Midrapidity Neutral-Pion Production in Proton-Proton Collisions at $\sqrt{s} = 200$ GeV, *Phys. Rev. Lett.* **91**, 241803 (2003).
- [35] A. Adare *et al.* (PHENIX Collaboration), Centrality dependence of low-momentum direct-photon production in $Au + Au$ collisions at $\sqrt{s_{NN}} = 200$ GeV, *Phys. Rev. C*

- 91**, 064904 (2015).
- [36] S. S. Adler *et al.* (PHENIX Collaboration), Measurement of Direct Photon Production in $p + p$ Collisions at $\sqrt{s} = 200$ GeV, Phys. Rev. Lett. **98**, 012002 (2007).
- [37] A. Adare *et al.* (PHENIX Collaboration), Direct photon production in $p + p$ collisions at $\sqrt{s} = 200$ GeV at midrapidity, Phys. Rev. D **86**, 072008 (2012).
- [38] T. Sjöstrand, S. Mrenna, and P. Skands, PYTHIA 6.4 physics and manual, JHEP **2006** (05), 026.
- [39] S. Zhang *et al.*, Extraction of inclusive photon production at mid-rapidity in $p + p$ and Au + Au collisions at $\sqrt{s_{NN}} = 200$ GeV, NUCL SCI TECH **32**, 7 (2021).
- [40] L. Adamczyk *et al.* (STAR Collaboration), Energy dependence of acceptance-corrected dielectron excess mass spectrum at mid-rapidity in Au+Au collisions at $\sqrt{s_{NN}} = 19.6$ and 200 GeV, Phys. Lett. B **750**, 64 (2015).
- [41] G. Agakichiev *et al.* (CERES Collaboration), e^+e^- -pair production in Pb-Au collisions at 158 GeV per nucleon, Eur. Phys. J. C **41**, 475 (2005).
- [42] J. Adam *et al.* (STAR Collaboration), J/ψ production cross section and its dependence on charged-particle multiplicity in $p + p$ collisions at $\sqrt{s} = 200$ GeV, Phys. Lett. B **786**, 87 (2018).
- [43] A. Adare *et al.* (PHENIX Collaboration), Transverse momentum dependence of J/ψ polarization at midrapidity in $p + p$ collisions at $\sqrt{s} = 200$ GeV, Phys. Rev. D **82**, 012001 (2010).
- [44] K. Saraswat, P. Shukla, and V. Singh, Transverse momentum spectra of hadrons in high energy pp and heavy ion collisions, J. Phys. Commun. **2**, 035003 (2018).
- [45] T. S. Biró, G. Purcsel, and K. Ürmösy, Non-extensive approach to quark matter, Eur. Phys. J. A **40**, 325 (2009).
- [46] C. Tsallis, Possible generalization of Boltzmann-Gibbs statistics, J. Statist. Phys. **52**, 479 (1988).
- [47] L. Adamczyk *et al.* (STAR Collaboration), J/ψ polarization in p+p collisions at $\sqrt{s} = 200$ GeV in STAR, Phys. Lett. B **739**, 180 (2014).
- [48] M. Bedjidian *et al.*, hep-ph/0311048 and R. Vogt private communication (2004).
- [49] D. J. Lange, The EvtGen particle decay simulation package, Nucl. Instrum. Meth. A **462**, 152 (2001).
- [50] J. Adam *et al.* (STAR Collaboration), Measurement of inclusive J/ψ polarization in $p + p$ collisions at $\sqrt{s} = 200$ by the STAR experiment, Phys. Rev. D **102**, 092009 (2020).
- [51] P. Wang, Υ measurements in Au + Au collisions at $\sqrt{s_{NN}} = 200$ GeV from STAR Experiment, Ph.D. thesis, University of Science and Technology of China (2021).
- [52] L. Adamczyk *et al.* (STAR Collaboration), Di-electron spectrum at mid-rapidity in $p + p$ collisions at $\sqrt{s} = 200$ GeV, Phys. Rev. C **86**, 024906 (2012).
- [53] C. Aidala *et al.* (PHENIX Collaboration), Measurements of $\mu\mu$ pairs from open heavy flavor and Drell-Yan in $p + p$ collisions at $\sqrt{s} = 200$ GeV, Phys. Rev. D **99**, 072003 (2019).
- [54] W. Xu, *Non-Photonic Electron at High Transverse Momentum in Au+Au Collisions and Bottom Quark Production in p+p Collisions at $\sqrt{s_{NN}} = 200$ GeV*, Ph.D. thesis, University of California, Los Angeles (2012).
- [55] F. Si *et al.*, Charm and beauty isolation from heavy flavor decay electrons in Au+Au collisions at $\sqrt{s_{NN}} = 200$ GeV at RHIC, Phys. Lett. B **805**, 135465 (2020).